PERGAMON

International Journal of Heat and Mass Transfer 45 (2002) 1063–1075

International Journal of HEAT and MASS TRANSFER

www.elsevier.com/locate/ijhmt

Approach towards spatial phase reconstruction in transient bubbly flow using a wire-mesh sensor

S. Richter [a,*], M. Aritomi [a], H.-M. Prasser [b], R. Hampel [c]

[a] *Tokyo Institute of Technology, Research Laboratory for Nuclear Reactors, 2-12-2 Ohokayama, Meguro-Ku, 152-8550 Tokyo, Japan*
[b] *Research Center Rossendorf, Institute for Safety Analysis, Postfach 51-01-19, 01314 Dresden, Germany*
[c] *University of Applied Science HTWS Zittau/Görlitz, Institute for Process Technique, Automation and Measuring Technique, Theodor-Körner-Allee 16, 02763 Zittau, Germany*

Received 17 January 2001; received in revised form 1 June 2001

Abstract

A wire-mesh sensor, which is based on local conductivity measurement, has been applied to studies on the characteristics of bubble flow in a rectangular channel (20×100 mm^2). Special design of the sensor allowed the measurement of the local instantaneous true gas velocity besides the measurement of the local instantaneous void fraction. A review of an already published method for true gas velocity measurement under consideration of the uncertainty caused by limitations in the sampling frequency is presented. A cluster-algorithm is proposed for the evaluation of bubble size distribution and volume flow reconstruction. The validity of this algorithm for spatial field reconstruction was benchmarked by theoretical considerations as well as comparison of the calculated with alternatively measured data. Good agreement was stated. The achieved information was used to obtain plots showing the bubble/slug velocity (up to the second statistical momentum) depending on the spherical-equivalent bubble diameter. This information was measured inside a transient bubble flow with void fraction of up to 20%. Occurring phenomena are explained by presented Fourier spectra of the cross-sectional averaged void fraction and the gas volume flow.

1. Introduction

Extensive studies on the characteristic behavior of the dispersed phase in a two-phase mixture supply information about the inside of such flows and enable us to increase the understanding of the physics, necessary for any kind of modeling. Particular interest is in the temporal and spatial distribution of the gaseous phase, its velocity and approximate shape since these quantities alter the exchanged momentum significantly and so not only the flow structure but also the heat and mass transfer characteristics.

In the past, several attempts have been made in order to achieve detailed information about the flow behavior of the dispersed phase by utilizing X-ray, capacitive, optical and conductive tomography. These techniques and the achieved result were reported in detail [1,3–6]. Although many approaches have been made, the success in order to evaluate the 3-dimensional characteristics of the dispersed phase in a two-phase mixture has been limited since the spatial resolutions of the applied sensors were at maximum of the order of 2–3 mm and the temporal resolution did not exceed significantly 1 ms [6]. Furthermore, the correct sharp representation of the interface still remains difficult [5]. In general, it has to be stated that the approaches made were not able to obtain an instantaneous picture of the spatial distribution of the dispersed field as well as its velocity. So up to now no data have been published showing the statistical characteristics of true gas velocities as a function of the volume contained in a void structure.

For the purpose of the local void fraction measurement, simultaneously at a high number of points in a cross-section A_c, Prasser et al. [3] proposed a wire-mesh sensor which was characterized by one measuring plane,

* Corresponding author. Tel.: +81-3-5734-3063; fax: +81-3-5734-2959.
E-mail address: richter@2phase.nr.titech.ac.jp (S. Richter).

0017-9310/02/$ - see front matter
PII: S0017-9310(01)00211-3

Nomenclature

A_c	cross-section (1 m^2)
A^f	Fourier amplitude (various)
D	standard deviation (various)
d_B, D_B	bubble diameter, bubble diameter class (1 m)
E	mean value (various)
f	functional relationship (dimensionless)
f	frequency (1 Hz)
$\mathscr{F}\{\}$	Fourier transformed (dimensionless)
u_G, U_G	superficial gas velocity, instantaneous, time averaged (1 m/s)
p	pressure (1 Pa)
p	p.d.f. (dimensionless)
$\tilde{p}_u$	p.d.f., equidistant in velocity classes (dimensionless)
$\tilde{\tilde{p}}$	p.d.f., locally restricted to uncertainty (dimensionless)
P	probability (dimensionless)
$\vec{r}$, $\vec{s}$	vectors in space R^3 (1 m)
t	time (1 s)
T	duration, time class (1 s)
T	temperature (1 K)
U_{el}	voltage (1 V)
$u_{G,G}$, $U_{G,G}$	true velocity, instantaneous, time averaged (1 m/s)
U_i	velocity class, general (1 m/s)
$\tilde{U}_i$	velocity class, equidistant (1 m/s)
V	volume (1 m^3)
x_1, x_2	coordinates in the cross-section (1 m)
Φ^ε	distribution function (dimensionless)
Φ^u	ramp event (dimensionless)
ε	void fraction (dimensionless)
δ	delay frames (dimensionless)
Δ_W	distance between the WMS measuring planes (1 m)

Superscripts

0	normalized or referring standard condition
A	referring air
k, κ	list counter
w	referring water
ε	referring void

Subscripts

δ	referring delay frame number
ε	referring void fraction
B	referring bubble
i, j, k, l, m, n, o	counting variables
LFM	referring laminar flow meter
max	maximum
sph	spherical (equivalent)
T	referring time delay
U	referring velocity
video	referring video
w	referring wire-mesh sensor
$X1$, $X2$	referring coordinates in the cross-section

256 measuring points, a sampling rate of 1024 Hz and the main feature that due to single-point sampling any phase reconstruction from obtained projections by post-processing has been avoided. The simplicity of the device stimulated the authors to make use of a slightly modified version of the proposed sensor, equipped with two of the above-mentioned measuring planes in order to achieve information about the local instantaneous gas velocity besides the data of instantaneous local void fraction [6,7].

The successfully reported application of a wire-mesh tomograph for the measurement of the local true gas velocity $u_{G,G}$ [6,7] was motivation to promote efforts towards a spatial reconstruction of the bubble field that passed through such a device. In particular, there was a strong interest to achieve data about the bubble size distribution depending on the statistically expected rising velocity in the flow. It was motivated by the demand for the verification of Euler–Lagrange models. Furthermore, the possible applicability of the wire-mesh sensor for approximate evaluation of the gas volume flow should have been checked.

1.1. The applied wire-mesh sensor, WMT

The applied wire-mesh sensor was originally proposed by Prasser et al. [3,4], and is described here in brief: The principle is based on the local conductivity measurement between the gap of a crossed electrode pair (90°). The simplified electrical scheme is illustrated in Fig. 1 for a 4×4 electrode device.

The principle works as follows [3]: The horizontally drawn transmitter wires (Fig. 1) are successively activated by a multiplex circuit closing the switches S1–S4, sequentially. To avoid electrolysis, which certainly would alter the measured results significantly, the potential on the temporarily activated transmitting wire is inverted once each half excitation period by switching SP. One excitation period is defined as the duration and one of the switches (S1–S4) is continuously closed. It is possible to change the sign of the supplied potential since the conductivity measurement does not depend on the direct current. Switching SP yields a supplied voltage on the electrodes, which are rectangular in shape. This excitation of a single transmitter wire causes a current in

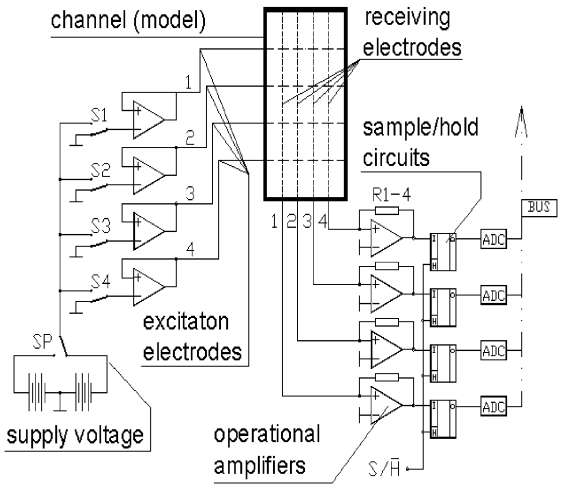

Fig. 1. WMT, simplified electrical scheme.

the scanned receiving wire (vertically drawn in Fig. 1). Since all receiver wires are scanned separately, each crossing-point of transmitter and receiver electrodes is scanned individually. The resulting current is transformed into voltage by a resistance R1–R4 and amplified by operational amplifiers, one for each receiver. The signal is temporarily kept by individual sample/hold circuits. To distinguish between the current that is caused by the influence of the capacity along the active electrodes and the corresponding load separation in the fluid, and the current that is a function of the local conductivity in a closed region around the crossing-point, the sample/hold circuits are released by the switch S/H after a stable voltage level is reached. The released signal is 12 bit AD converted and stored in a data acquisition computer. Signals are stored for each receiver separately.

Utilized electrodes have a diameter of 0.1 mm. They are manufactured of stainless steel and are arranged equidistantly in three planes, separated 1.5 mm in the main flow direction and resolving 2.2×3.03 mm^2 over an entire cross-section of 20×100 mm^2 (Fig. 2(a)). Three realized planes of wires yield two planes of cross-points. These so-called measuring planes are supposed to be centered between the electrode planes. The measuring volume is defined by the fact that electrode crossing-points are scanned individually while the electrical potential of all the remaining non-scanned wires is kept to zero [3,6]. This has been realized by electrodes, which are equipped with an impedance significantly lower than that of water. So the influence of the phase distribution outside the observing point is excluded. For the conversion between measured local conductivity and the void fraction ε, a linear approach was proposed [3] neglecting the deformation of the electromagnetic field around the crossing-point in first-order:

$$\varepsilon(\vec{r},t) = \varepsilon(t)_{x_1,x_2} = \frac{(U_{\mathrm{el}}(t))_{x_1,x_2} - (U_{\mathrm{el}}(t)^{\mathrm{W}})_{x_1,x_2}}{(U_{\mathrm{el}}(t)^{\mathrm{A}})_{x_1,x_2} - (U_{\mathrm{el}}(t)^{\mathrm{W}})_{x_1,x_2}}. \quad (1)$$

The measurement of the cross-sectional and time averaged void fraction by this method has been found within 1% accuracy compared to data, alternatively obtained by X-ray tomography [3]. The accuracy for the local value was concluded to be of the same order [3].

2. Analysis

Since the electrical potential over the entire cross-section except for the measuring point is kept zero, the measuring volume can be defined as of the size of one mesh centered at the electrode crossing-point [6]. As il-

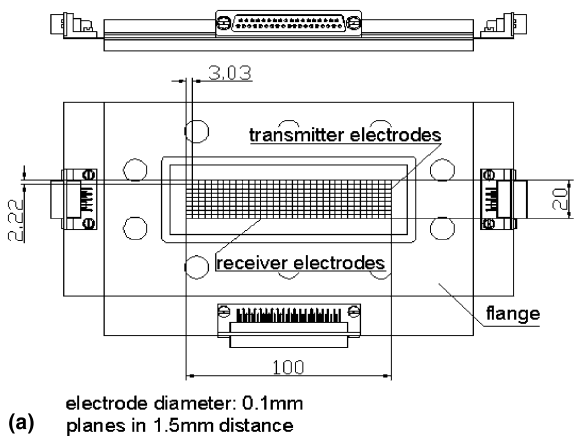

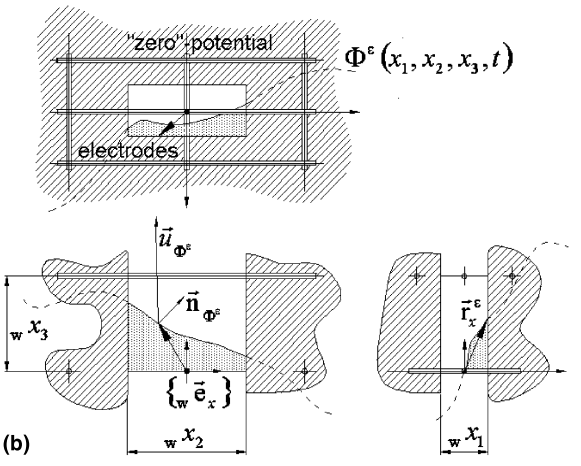

Fig. 2. Wire-mesh sensor: (a) layout of the applied device; (b) averaging over a single electrode crossing-point.

lustrated in Fig. 2(b), the volume is of the dimension ${}_{\mathrm{W}}x_1$ and ${}_{\mathrm{W}}x_2$ in the x_1- and x_2-directions, respectively (2.22×3.03 mm^2). Its height is given by the distance between the electrode planes Δ_{W} (1.5 mm). Assuming a time dependent spatial distribution of the gaseous phase that is indicated by a function $\Phi^{\varepsilon}: \Phi^{\varepsilon}$ (gas) $= 1$, Φ^{ε} (liquid) $= 0$, the time dependent void fraction averaged within the measuring volume, ${}_{\mathrm{W}}\varepsilon({}_{\mathrm{W}}t)$, writes:

$$ {}_{\mathrm{W}}\varepsilon({}_{\mathrm{W}}t) = \frac{1}{{}_{\mathrm{W}}x_1\,{}_{\mathrm{W}}x_2\,{}_{\mathrm{W}}x_3} \int_{x_1=0}^{{}_{\mathrm{W}}x_1} \int_{x_2=-({}_{\mathrm{W}}x_2/2)}^{({}_{\mathrm{W}}x_2/2)} \times \int_{x_3=-({}_{\mathrm{W}}x_3/2)}^{({}_{\mathrm{W}}x_3/2)} \Phi^{\varepsilon}(x_1, x_2, x_3, {}_{\mathrm{W}}t)\,\mathrm{d}x_1\,\mathrm{d}x_2\,\mathrm{d}x_3. \quad (2) $$

Since every crossing-point is scanned individually, the available sampling time per volume has a duration of T_{W}. The measuring principle requires that the influence of the conductivity distribution around the measuring points has to be distinguished from the influence of the capacitance. For this purpose a stationary value, achieved within T_{W}, is used. It is defined as an average over T_{W}.

With respect to the fact that T_{W} is about three-orders lower than the characteristic sample duration of the WMT, as well as that a spatial resolution of 2.22×3.03 mm^2 is small enough compared to the channel-dimension, the evaluated value of ${}_{\mathrm{W}}\bar{\varepsilon}^{T_{\mathrm{W}}}$ will be understood as the local instantaneous void fraction $\varepsilon(\vec{r}, t)$ (being aware that it is defined by a spatial average over ${}_{\mathrm{W}}x_1$, ${}_{\mathrm{W}}x_2$, ${}_{\mathrm{W}}x_3$ and some time average within T_{W}):

$$ {}_{\mathrm{W}}\bar{\varepsilon}^{T_{\mathrm{W}}} = \varepsilon(\vec{r}, t) = \frac{1}{T_{\mathrm{W}}} \int_{{}_{\mathrm{W}}t=0}^{T_{\mathrm{W}}} {}_{\mathrm{W}}\varepsilon({}_{\mathrm{W}}t)\,\mathrm{d}_{\mathrm{W}}t. \quad (3) $$

A similar result could have been reached with a suitably defined filter function.

2.1. Review: velocity measurement

The utilized method to measure the true gas velocity $u_{\mathrm{G,G}}$ is explained here in brief. It is reported in Richter et al. [6,7].

The fact that the signal which a bubble causes at the two measuring planes is statistically similar as shown in Figs. 4(b) and (d) enables us to use a delay time measurement between two certain identifiers in order to evaluate the velocity of an approaching interface. As a certain identifier the positive [1] ramp event Φ^{u}_{pos} has been introduced, i.e. a jump in the (noise free) local void fraction ε, Fig. 3, from zero to a larger value within dt [6]:

[1] The negative ramp event Φ^{u}_{neg} has not been utilized: Fig. 4 shows that there is an alteration of the downstream signal – resulting from void shape alteration by the electrode wires and thereby to evaluate the surface velocity.

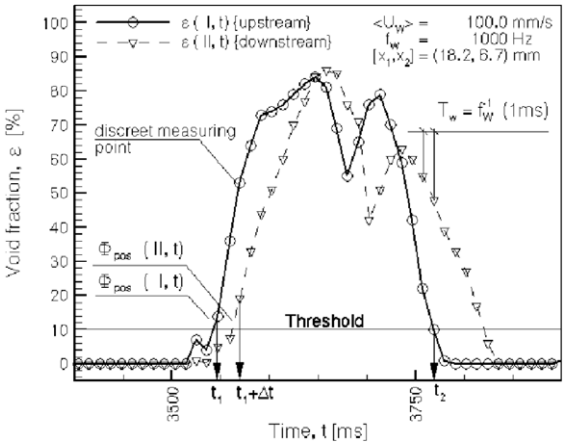

Fig. 3. Void fraction signal, local signal course.

$$ \Phi^{u}_{\mathrm{pos}}(\vec{r}, t) = (\varepsilon(\vec{r}, t) = 0) \cap (\varepsilon(\vec{r}, t + \mathrm{d}t) > 0). \quad (4) $$

The delay time between two of such ramps Φ^{u}_{pos}, occurring at two locations that are separated by the distance $|s|$ is used to evaluate the velocity of the surface $u_{\mathrm{G,G}}$ within $|s|$. To ensure that the signal is caused by one and the same bubble, a further condition has been proposed [6,7]:

$$ \Delta t : \Phi^{u}_{\mathrm{pos}}(\vec{r}, t) \cap \Phi^{u}_{\mathrm{pos}}(\vec{r} + \vec{s}, t + \Delta t) \cap \left[\underset{\delta t=0}{\overset{\Delta t}{\forall}} : \varepsilon(\vec{r}, t + \delta t) > 0 \right]. \quad (5) $$

Utilizing such a delay time Δt implies that there is a maximal measurable velocity $u_{\max}$ defined by the WMT sampling rate f_{W} and the distance $|s|$, i.e. the distance in between the measuring planes Δ_{W}:

$$ u_{\max} = \Delta_{\mathrm{W}} f_{\mathrm{W}}. \quad (6) $$

In general, velocities are evaluated depending on the number of delay frames (i.e. number of samples) δ

$$ u_{\delta} = \frac{\Delta_{\mathrm{W}} f_{\mathrm{W}}}{\delta} \quad (7) $$

The value of u_{δ}, Eq. (7), is characterized by an uncertainty U_{δ} [6]

$$ U_{\delta} = \frac{\Delta_{\mathrm{W}} f_{\mathrm{W}}}{\delta(\delta + 1)}. \quad (8) $$

Due to the uncertainty in the velocity evaluation U_{δ} it comes that a p.d.f., $p_{u\delta}$, appears algebraically stretched if it is plotted over equidistant velocity arguments [6,7]. From the physical point of view, the rising velocity of bubbles oscillates around a mean value due to surface deformation and interaction with the liquid turbulence. Even though the exact statistical behavior is rather unknown, there is an evidence that it behaves sufficient smoothly [1,2,8]. Facing this Lagrangian point of view,

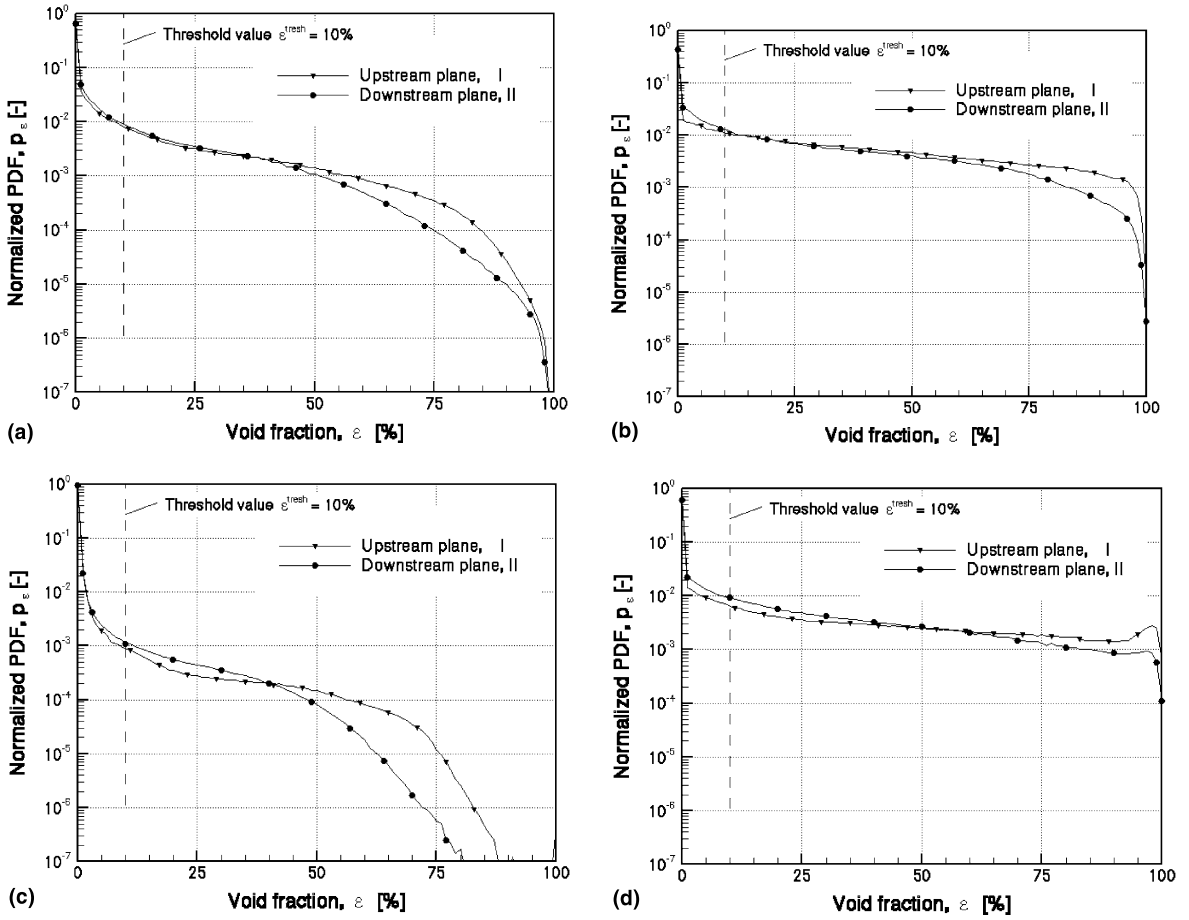

Fig. 4. P.d.f. of occurring void fraction levels: (a) $\langle U_L \rangle = 0$ mm/s, $\langle U_G \rangle = 2.5$ mm/s; (b) $\langle U_L \rangle = 110$ mm/s, $\langle U_G \rangle = 2.5$ mm/s; (c) $\langle U_L \rangle = 0$ mm/s, $\langle U_G \rangle = 10$ mm/s and (d) $\langle U_L \rangle = 100$ mm/s, $\langle U_G \rangle = 10$ mm/s.

it can be assumed that inside an Eulerian framework there will be at a certain point in space no discontinuity in the p.d.f. that describes the true gas velocity. Insofar it has been proposed that a certain normalized occurrence frequency $p_{u\delta}$ is replaced by a redistributed function $\tilde{p}_u$ that does not show singularities but is characterized by the same probability value for a measurable velocity u_δ, $P(u_\delta)$, and sufficient in temporal resolution, Eq. (8). This is done by assuming delay time events distributed by $\tilde{\tilde{p}}$ within the uncertainty range U_δ [6]:

$$\sum_{\{\delta\}} p_{u\delta} U_\delta = \sum_{\{j\}} \tilde{p}_{uj} \tilde{U}_j = \sum_{\{\delta\}} \sum_{\{k\}} \tilde{\tilde{p}}_{uk} p_{u\delta} U_\delta. \tag{9}$$

In the first instance, $\tilde{\tilde{p}}$ has been supposed to be constant over and normalized in U_δ.

The p.d.f. changes its appearance as illustrated by Fig. 5. The achieved accuracy in the prediction of the true gas velocity (up to the second statistical moment)

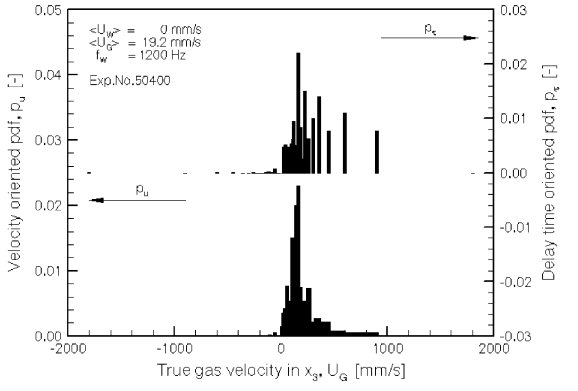

Fig. 5. True gas velocity p.d.f. in measured (upper half) and redistributed appearance (lower half).

can be stated as within ±5% in comparison to video data, for velocities of $U_{G,G} < 500$ mm/s as shown in Fig. 6(a).

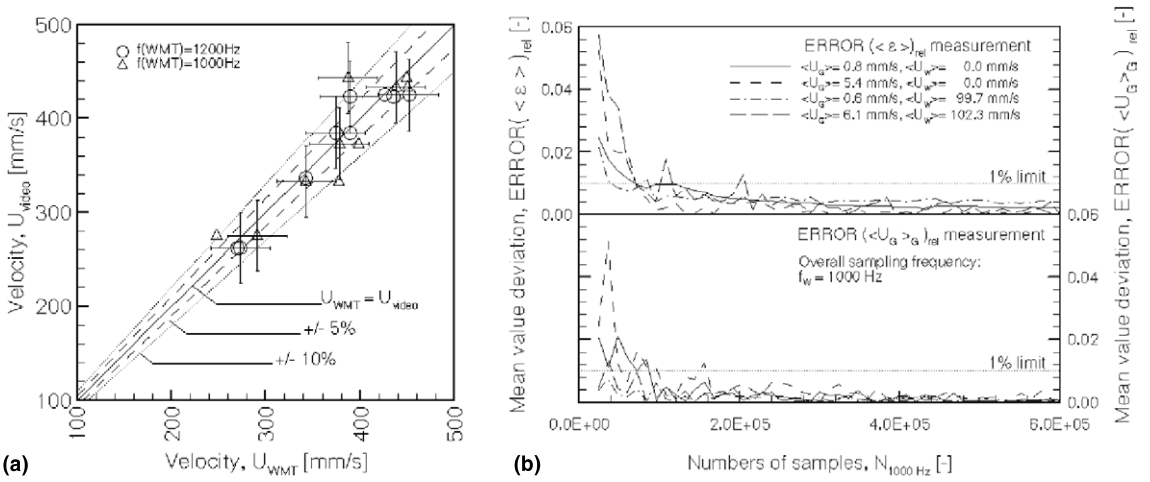

Fig. 6. Accuracy and certainty: (a) WMT-measured true gas velocities, $(U_{G,G})_{WMT}$, compared to high-speed video observations, $(U_{G,G})_{video}$; (b) certainty in the estimation of cross-sectional time averaged void fraction, $\langle\varepsilon\rangle$, (upper half) and true gas velocity, $\langle U_{G,G}\rangle$, (lower half).

Fig. 6(b) shows the uncertainty in the calculation of the mean value for $\langle\varepsilon\rangle$ and $\langle U_{G,G}\rangle$ in its dependency on the sampling duration. The measuring time has been chosen suitable to achieve a certainty higher 99% for the calculated statistical moments and all data presented in this paper.

2.2. Spatial field reconstruction

The simultaneously obtained information about the true gas velocity $u_{G,G}(t)$ and the local void fraction $\varepsilon(t)$ suggests the spatial reconstruction of the dispersed phase from the slice-wise produced projection of a bubble on the WMT measuring plane. Since the velocity of a gas-filled void can only be determined by the velocity of its interface, it has to be supposed that this velocity is representative for the entire structure. This requires in particular an interface which migrates with a constant velocity that is not altered by an interaction with the electrode wires. The validity of this requirement is discussed later.

To detect a continuous void structure, a list $\mathbf{L}\varepsilon$ has been introduced. This list $\mathbf{L}\varepsilon^k$ contains all measured void fraction values in an x_1, x_2, t – space that have a continuous connection to each other at the clustering step k. The elements are defined by Eq. (10) and implemented by a recursive formula, calling itself under variation of the coordinates (x_1, x_2, t) over a 6-point stencil:

$$L\varepsilon_i^{k+1}\begin{pmatrix}\tilde{x}_1\\ \tilde{x}_2\\ \tilde{t}\end{pmatrix} := \overset{1}{\underset{m=0}{\forall}} : \overset{1}{\underset{n=0}{\forall}} : \overset{1}{\underset{o=0}{\forall}} : L\varepsilon_j^k\begin{pmatrix}x_1+1-2m\\ x_2+1-2n\\ t+1-2o\end{pmatrix} > 0 \cap L\varepsilon_i^{k+1} \notin L\varepsilon_l^{\kappa} : \kappa \in [0,k+1]. \tag{10}$$

With the integral value of $\mathbf{L}\varepsilon$ and the evaluated true velocity $u_{G,G}$, the void volume writes at thermodynamic standard condition p^0, T^0:

$$V_B^0 = \frac{p}{p^0}\frac{T^0}{T}\Delta x_1\Delta x_2\Delta_W \sum_{\{V_B\}}\varepsilon\left|\frac{1}{\delta}+\int_{T_{\delta-1}}^{T_\delta}\tilde{\tilde{p}}\,\mathrm{d}t\right| = \frac{p}{p^0}\frac{T^0}{T}\Delta x_1\Delta x_2\Delta_W \sum_{\{V_B\}}\varepsilon\left|\frac{1}{\delta}+\frac{1}{2\delta(\delta+1)}\right|. \tag{11}$$

It should be noted that the instantaneous gas velocity $u_{G,G}$ is supposed to be the mean value within the uncertainty range U_δ for the purpose of bubble volume reconstruction. This can be seen in the integral over $\tilde{\tilde{p}}$ in Eq. (11) that simplifies if $\tilde{\tilde{p}}$ is constant within U_δ to the last term on the r.h.s. Since the real value of $u_{G,G}$ remains unknown, huge errors in U_G are possible for high values of $u_{G,G}$ (i.e. small δ).

2.3. Characteristics, accuracy and certainty

The quality of the clustering algorithm, Eqs. (10) and (11) can be assessed, if a maximum measured void fraction value ε_{max} belonging to a volume V_0^B is within a margin that was achieved by theoretical considerations. The influence of an arbitrary distribution of gas in the measuring volume (Fig. 2(b)) on the measured void fraction can be visualized by this consideration.

If a bubble of the diameter d_B enters the measuring volume defined by ${}_Wx_1$, ${}_Wx_2$, ${}_Wx_3$, it causes a void fraction ε that is a function of the bubble diameter d_B and the bubble position, in general expressed by a vector r_x^ε. Such functional relationship f^ε is defined by Eq. (12):

$$f^\varepsilon : r_x^\varepsilon, d_B \mapsto \varepsilon | \varepsilon \in R,[0,1]. \tag{12}$$

In cylindrical coordinates r, θ, z, the relation f^{ε} writes:

$$f^{\varepsilon} = \frac{1}{{}_{\mathrm{W}}x_1\,{}_{\mathrm{W}}x_2\,{}_{\mathrm{W}}x_3} \times \int_{r=0}^{\min\{|({}_{\mathrm{W}}x_1/2)(\cos\theta)^{-1}|,|({}_{\mathrm{W}}x_2/2)(\sin\theta)^{-1}|,\sqrt{(d_{\mathrm{B}}/2)^2-r^2}\}} \times \int_{\theta=0}^{2\pi} \int_{z=-\min((d_{\mathrm{B}}/2),({}_{\mathrm{W}}x_3/2))}^{\min((d_{\mathrm{B}}/2),({}_{\mathrm{W}}x_3/2))} r\,\mathrm{d}r\,\mathrm{d}\theta\,\mathrm{d}z. \quad (13)$$

The function values of f^{ε} become extreme for a constant displacement in the x_3-direction, if the bubble moves directly at the electrode crossing-point (i.e. $x_1 = 0$, $x_2 = 0$) or in the center of the cell-center, i.e. centered between four electrode-crossing-points (i.e. $x_1 = {}_{\mathrm{W}}x_1/2$, $x_2 = {}_{\mathrm{W}}x_2/2$). Suppose that there is no influence of the void distribution Φ^{ε} on the measured void fraction ε, every evaluated bubble diameter d_{B}, Eq. (11), should be characterized by the fact that the generating list $\mathbf{L}\varepsilon$ contains a void fraction maximum $\varepsilon_{\max}$, lying between the above two theoretically derived extreme values [9]. Considered lists $\mathbf{L}\varepsilon$ were of significant higher dimension than 1.

A numerical solution of Eq. (13) for a mesh size of 2.22×6.06 mm^2 as well as the fit of experimental data can be seen in Fig. 7(a).

The data for $\varepsilon_{\max}$ within $\mathbf{L}\varepsilon$ fit the theoretically expected interval well. The slight deviation at larger arguments of D_{B} was explained by the formation of water-lips. These water structures prevent the electrodes to be completely covered with gas and so cause an artificial reduction of the measured void fraction ε [9]. At the very right of Fig. 7(a), at void fraction values of $\varepsilon_{\max} \sim 55\%$, there is a small agglomeration of points. This is supposed to be caused by a failure of the clustering algorithm (“jumping”): if two bubbles move at very short distance, e.g. before coalescence or after fragmentation, the algorithm is not able to distinguish between them. However, it is noteworthy that even though the volumetric bubble density was comparatively high in such a regime (of up to $\langle\varepsilon\rangle \sim 20\%$), the spatial resolution of the WMT was fine enough to separate these continuities from the homogeneous phase.

A further interesting point is to question if there might be a relation between the time derivatives of the time dependent void fraction course, illustrated in Fig. 2(a) and the velocity evaluated by the delay time analysis proposed by Eqs. (2)–(9). In order to achieve some generality in such an analysis, the dependency on d_{B} and $u_{\mathrm{G,G}}$ has been removed introducing suitable non-dimensional coordinates. The void fraction has been replaced by ε^0 due to normalization with the maximum $\varepsilon_{\max}$ of the generating list $\mathbf{L}\varepsilon : \varepsilon^0 = \varepsilon/\varepsilon_{\max}$. The time was Galilean transformed, i.e. divided by the ratio between $u_{\mathrm{G,G}}$ and ${}_{\mathrm{W}}x_3 : t^* = tu_{\mathrm{G,G}}/\Delta_{\mathrm{W}}$. Utilizing f^{ε}, Eq. (13), the non-dimensional void fraction time derivative $f^{\varepsilon^0}_{,t^*}$ writes:

$$f^{\varepsilon^0}_{,t^*} = \varepsilon^0_{,t^*} = \frac{\partial\left(\frac{f^{\varepsilon}(\vec{r},t)}{f^{\varepsilon}(0,0)}\right)}{\partial t^*}. \quad (14)$$

A comparison with experimentally obtained data shows that the so-generated functions envelop the experimental data set, Fig. 7(b). There are almost no data outside the theoretically predicted enveloping set of functions. So it can be concluded that there might be some tendency for a slight deceleration, however, at present no quantitative assessment has been found. The simultaneously obtained information about the local void fraction ε and true gas velocity $u_{\mathrm{G,G}}$ suggests further to calculate the local superficial gas velocity:

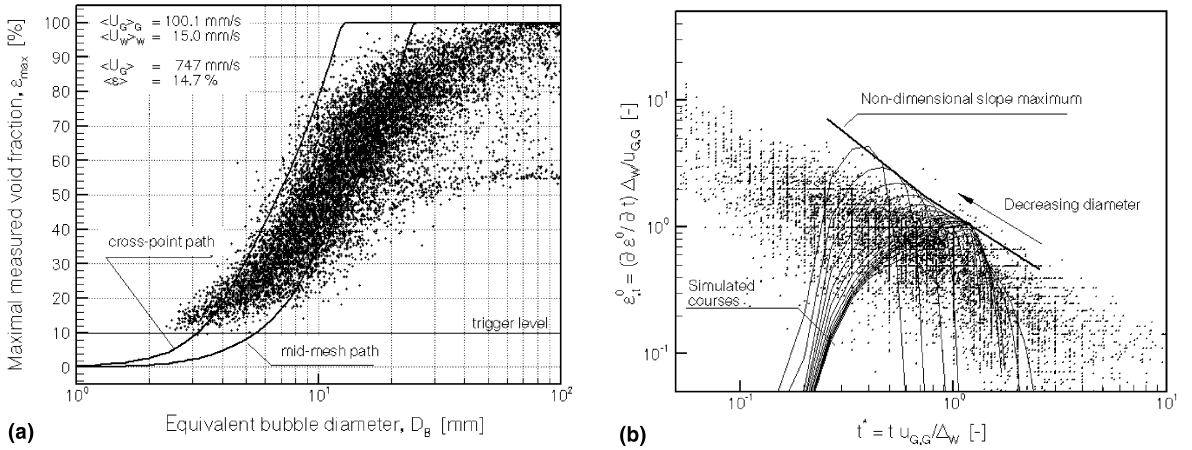

Fig. 7. Cluster-algorithm: (a) simulated and measured $\varepsilon_{\max} = \varepsilon_{\max}(D_{\mathrm{B}})$; (b) measured time gradients of the $\varepsilon(t)$-course in comparison to theoretically predicted enveloping functions.

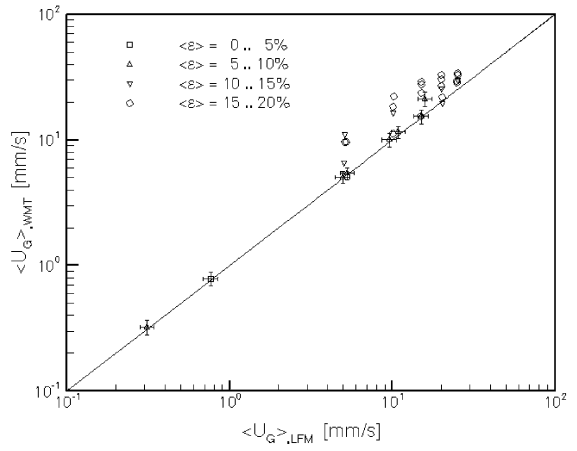

Fig. 8. Reconstructed time cross-sectional averaged superficial velocities $\langle U_G \rangle_{WMT}$ in comparison to LMF obtained data, $\langle U_G \rangle_{LFM}$.

$$\underset{\{t \in \{B\}\}}{\forall :} u_G(x_1, x_2, t_0 + t) = \varepsilon(x_1, x_2, t_0 + t) u_{G,G}(\varepsilon(x_1, x_2, t_0)). \tag{15}$$

It must be aware that the assumption of a constant bubble velocity while the void is passing the sensor, as well as the above-mentioned influence of the uncertainty in the velocity evaluation, U_δ, influences the result of the u_G measurement.

A qualitative assessment of the applicability of Eq. (15) can be seen in Fig. 8, where reconstructed data of the time cross-sectional averaged superficial gas velocity $(U_{G,G})_{WMT}$ are plotted against data, alternatively obtained by a laminar flowmeter LFM.

It can be stated that the order of the volume flow rate is correctly reproduced over three-orders of the flow rate. The void fraction ranges from almost $\varepsilon \sim 0\%$ up to $\varepsilon \sim 20\%$. However, an exact analysis of occurring errors in Fig. 9(a) indicates that there is a strong dependency on the true gas velocity $U_{G,G}$. At large values of $U_{G,G}$ the sensor overestimates the flow rate. Data scatter almost proportionally to the increase of $U_{G,G}$. There is nearly no underprediction. The reason therefore is seen in the large uncertainty in the true gas velocity evaluation resulting from the limitation in the sampling rate f_W. Values characterized by a true gas velocity $u_{G,G}$ lower than 250 mm/s show almost no deviation from the alternatively measured data. The uncertainty in the velocity prediction is lower than 12.2%, Eq. (8), and since $u_{G,G} \sim V_B^0 \sim u_G$ this uncertainty directly influences the volume flow prediction. u_G-values based on a true gas velocity that ranges within 250 mm/s $< u_G,\ G \leqslant 500$ mm/s show deviations of up to 10%, Fig. 9(b). These values have an uncertainty in the velocity prediction of up to 21.7%. This confirms the proposed linear interpolation of $\tilde{\tilde{p}}$ within U_δ [2] to a certain degree.

As illustrated in Fig. 9(a), occurring deviations in the volume flow rate prediction are almost independent of the void fraction level that ranges from $\varepsilon = 0$ to 20%. Insofar it can be concluded that significant improvement of the data shown in Fig. 9(a) will take place as soon as the overall sampling frequency of the wire-mesh sensor, f_W, increases. So it has to be expected that the application of the recently presented new wire-mesh tomograph [4] characterized by a sampling frequency of about 10,000 Hz will be able to make volume flow predictions within a 10% margin correctly for true gas velocities of up to 3750 mm/s (based on the same sensor and 20% uncertainty). Confirmation of this expectation will be the subject of near future research work.

3. Experimental results

The new layout of the sensor offers the opportunity to evaluate the local instantaneous gas velocity [6,7]. The accuracy up to the second-order statistical momentum has been found within ±5% as correct. This is of particular interest since up to now there has been no convenient possibility to investigate simultaneously the velocity of each individual bubble inside a turbulent bubbly flow. Furthermore, the spatial reconstruction of the dispersed phase in an Eulerian framework allows concluding on the bubble diameter spectrum. These two facts are interesting for the verification of Euler–Lagrangian models, where the statistical behavior of particles at a certain position within the continuous phase is necessary for a correct prediction of momentum and energy exchange.

Fig. 10 illustrates the obtained data as an example. The tests were carried out at a TIT/RLNR test loop that consists of a 20×100 mm^2 rectangular channel. The channel is vertically setup. It measures a length of 1580 mm. Due to modular design the sensor can be installed at arbitrary positions every 100 mm. The loop was designed for co-current air/water two-phase flow experiments at ambient conditions. The flow range can be controlled within $\langle U_L \rangle = 0$–250 mm/s, $\langle U_G \rangle = 0$–30 mm/s. Air is injected through 2 mm-steel needles, equipped with a 1 mm nozzle pointing in the main flow direction. The needles are individually adjustable in position and volume flow. For more details concerning

[2] Higher-order approximations have been investigated up to second-order. There was no significant change in the accuracy of predicted value for U_G, but the demand on computational power increased significantly. For that reason it has been refrained from further investigation in this direction.

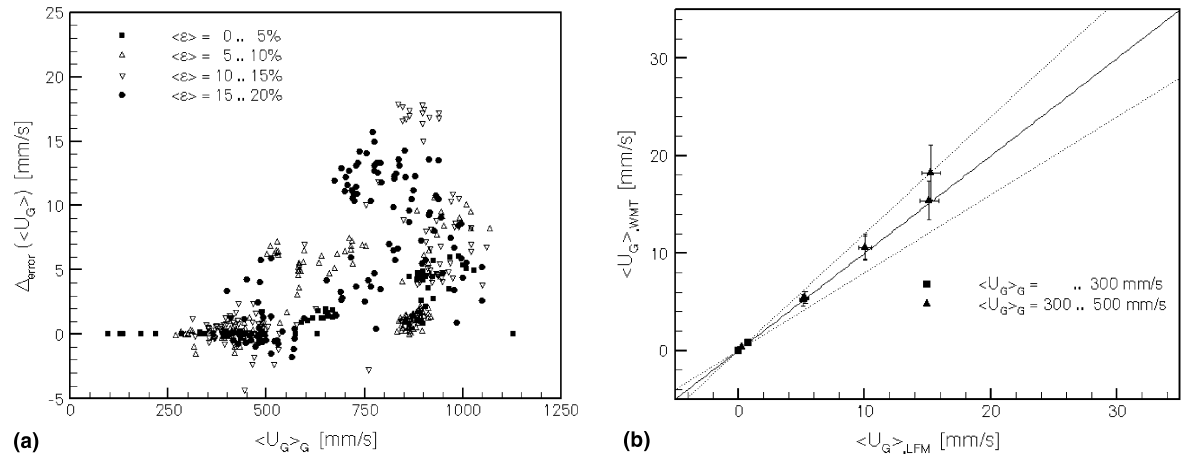

Fig. 9. Volume flow reconstruction: (a) $\langle U_G\rangle$-error dependency on $\langle\varepsilon\rangle$, $\langle U_G\rangle_G$; (b) $\langle U_G\rangle_{WMT}$–$\langle U_G\rangle_{LFM}$ – comparison at low velocities $\langle u_G\rangle_G$ with ±10% margin.

the experimental apparatus and additional instrumentation, see Richter et al. [6,7].

The referred experiment is based on a homogeneous air injection over the entire cross-section by 5 equidistantly installed needles at the channel-centerline. The water flow rate is kept constant at $\langle U_L\rangle \sim 100$ mm/s. The sensor has been installed 480 mm downstream the air injection needles. With this configuration, the time cross-sectional averaged void fraction has been stepwise increased.

Fig. 10 illustrates the bubble diameter spectrum (column I) as well as the contribution of a certain diameter class D_B to the integral void fraction. The plotted bubble diameter spectrum (upper half of the diagrams) is based on a p.d.f. that a certain bubble diameter D_B occurs

$$f_B(d_{B,sph}) = \left[\frac{\partial P(d_{B,sph} < D_B)}{\partial d_{B,sph}}\right]. \tag{16}$$

There is a clear tendency that with increasing $\langle\varepsilon\rangle$ the diameter of occurring small bubbles decreases in variation. Furthermore, there are a very few large bubbles developing with increasing $\langle\varepsilon\rangle$, which is a result of successive increasing coalescence.

The formulation in Eq. (16) has the disadvantage that only the detected bubble number is considered. There is no information as to how much each bubble diameter class D_B contributes to the integral void fraction. For this reason Eq. (16) has been extended [3]

$$f_{B,\varepsilon}(d_{B,sph}) = \frac{\partial\varepsilon(D_B)}{\partial D_B} = \frac{6}{\pi D_B^3}\frac{\partial P(d_{B,sph} < D_B)}{\partial d_{B,sph}}. \tag{17}$$

With the formulation proposed by Eq. (17), it can be clearly distinguished how much each bubble diameter class D_B is contributing to a given void fraction $\langle\varepsilon\rangle$. In Figs. 10(a)–(d) (column I), it can be clearly seen that with increasing gas flow, the amount of gas is more and more transported in a less number of very large slugs (increase of $f_{B,\varepsilon}$ at high values of D_B). At very high void fraction of $\langle\varepsilon\rangle \sim 20\%$, Fig. 10(d) (column I) shows a bimodal distribution of $f_{B,\varepsilon}$. The formation of two characteristic bubble size classes – indicated by the bimodal distribution of bubble diameter – results from progressing bubble coalescence and the onset of slug formation. The formation of the bimodal bubble distribution has also been reported by Prasser et al. [3].

The main feature of the sensor can be seen in the fact that true gas velocity $u_{G,G}$ and bubble size, expressed by the spherical equivalent diameter d_B, can be measured simultaneously. So it is possible to provide plots which show the local mean value for the true gas velocities in their dependency on the size of the void structure. It should be explicitly highlighted that these values are measured within a highly turbulent flow field where all sizes of bubbles are simultaneously available This feature is exemplarily illustrated in Figs. 10(a)–(d) (column II): Bubbles in a flow of low void fraction, Fig. 10(a) (column I), $\langle\varepsilon\rangle = 3.9\%$, tend to behave almost similar to an isolated single bubble, showing a rising velocity that increases with increasing bubble diameter. An increase in the void fraction to $\langle\varepsilon\rangle = 9.9$, 15.6%, Figs. 10(b) and (c), respectively, indicates in column II that bubbles tend to homogenize their rising velocities over a wide range of diameters independent of D_B. It seems that at this flow regime, the bubble movement is mostly governed by the action of turbulence. However, small bubbles ($D_B < 2$–3 mm) still move with lower velocities. Previously reported data [6,7] suggest that this is due to the fact that this bubble size can mainly be found in a mostly closed region to the channel wall, where velocities are low and the action of turbulence is limited due to the increase in the

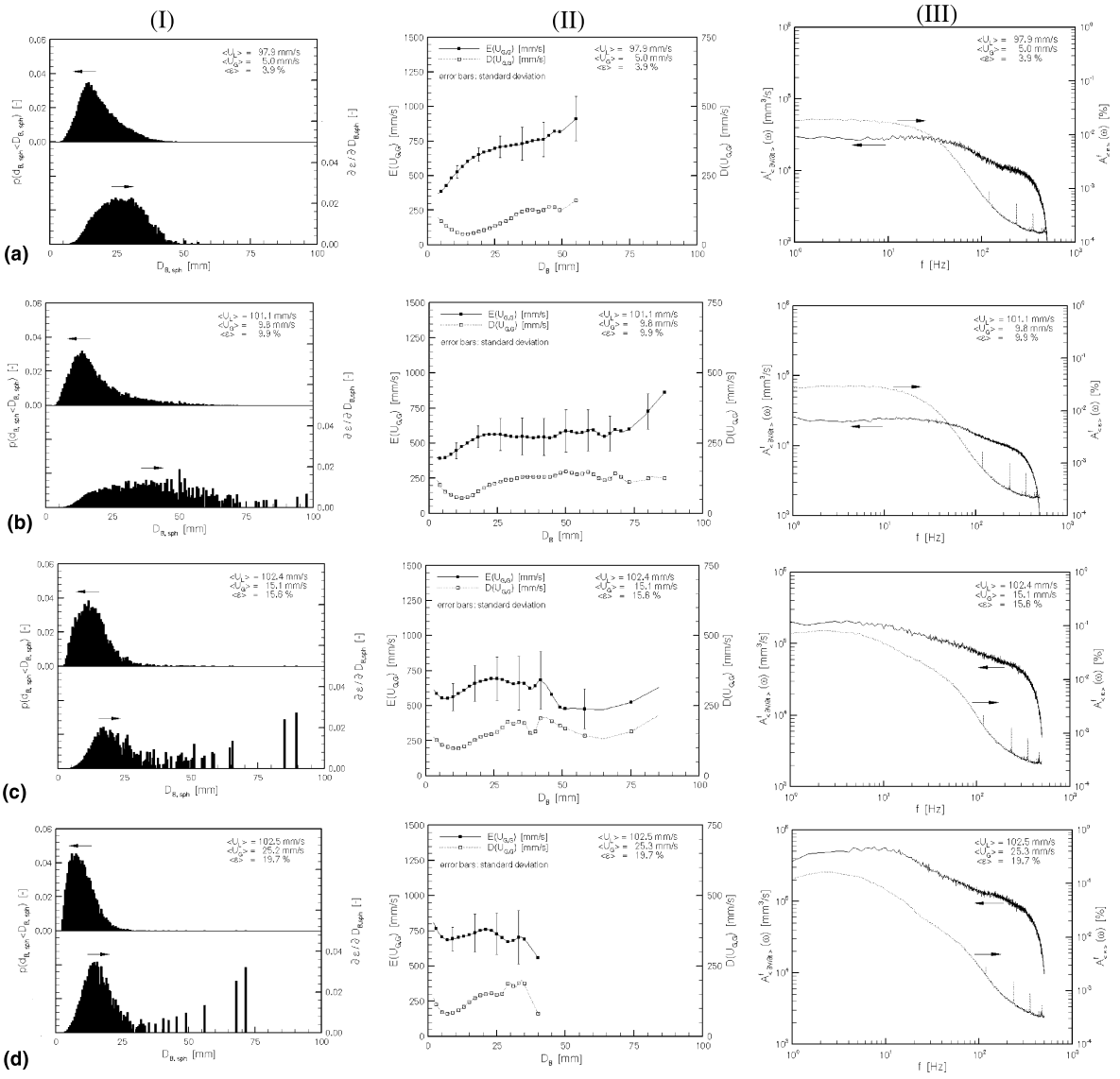

Fig. 10. Experimental example of D_B-spectrum (I), D_B–$u_{G,G}$-correlation (II), $\langle\varepsilon\rangle$–$\langle u_G\rangle$-spectrum (III) for: (a) $\langle U_L\rangle = 97.9$ mm/s, $\langle U_G\rangle = 5.0$ mm/s; (b) $\langle U_L\rangle = 101.1$ mm/s, $\langle U_G\rangle = 9.8$ mm/s; (c) $\langle U_L\rangle = 102.4$ mm/s, $\langle U_G\rangle = 15.1$ mm/s; (d) $\langle U_L\rangle = 102.5$ mm/s, $\langle U_G\rangle = 25.3$ mm/s.

viscous dissipation term. Oppositely, in the channel center, large bubbles were found [6,7]. In this region of high liquid velocity, developing small slugs ($D_B \sim 50$ mm/s) move with very high velocities and their velocity even increases with increasing equivalent diameter D_B. At a void fraction of $\langle\varepsilon\rangle \sim 20\%$, Fig. 10(d) (column II), there is some tendency that slugs were slowed slightly down. Even if the data for bubble diameter larger than $D_B \sim 25$ mm are highly uncertain due to the fact that most of the void is captured by some bubbles of extremely high diameter, Fig. 10(d) (column I), the tendency is obvious. The reason therefore is seen, based on visual flow observation, that slugs are deformed and move along a strongly curved trajectory through the channel. This alteration is caused by the action of recirculation vortices, which circulate smaller bubbles with high velocity and themselves move rather slowly in the main stream direction. Besides the alteration of the slug movement, the effective time average of U_G for small bubble diameters D_B reduces, since the relative component in main flow direction is altered by the circulation velocity.

To illustrate this mechanism at high $\langle\varepsilon\rangle$, the behavior of the instantaneous cross-sectional averaged void

fraction $\langle\varepsilon\rangle(t)$ as well as of the time-dependent cross-sectional averaged superficial velocity $\langle u_G\rangle(t)$, Eq. (15), has been analyzed in the frequency domain. Therefore, two Fourier-spectra are introduced

$$A^{f}_{\langle\varepsilon\rangle}(\omega) = \mathscr{F}\{\langle\varepsilon\rangle(t)\} = \int_{-\infty}^{+\infty}\left(\frac{1}{A_c}\sum_{\{x_1\}}\sum_{\{x_2\}}\varepsilon(x_1,x_2,t)\right)e^{-i\omega t}\,dt, \quad (18)$$

for the void fraction and

$$A^{f}_{\langle\partial V/\partial t\rangle}(\omega) = \mathscr{F}\{\langle u_G\rangle(t)\} = \int_{-\infty}^{+\infty}\left(\frac{1}{A_c}\sum_{\{x_1\}}\sum_{\{x_2\}}u_G(x_1,x_2,t)\right)e^{-i\omega t}\,dt, \quad (19)$$

for the superficial gas velocity.

The results of the frequency analysis can be seen in column III, Figs. 10(a)–(d). It should be noted that the measurements were carried out at a fixed position in an Eulerian frame. If a constant rising velocity $u_{G,G}$ is supposed, a small bubble results in rather peaking, a larger one in a comparatively stretched signal in time domain. In the frequency domain this means that at a unique velocity $u_{G,G}$ a signal of a large bubble will be shifted towards lower frequencies. The same effect can be observed, if a unique bubble diameter D_B is supposed and the velocity $u_{G,G}$ reduced.

The shape of $A^{f}_{\langle\varepsilon\rangle}$ seems to be independent of the void fraction at high frequencies f. However, the amplitude at low frequencies f increases with increasing $\langle\varepsilon\rangle$. The formation of a slight maximum can be observed, Figs. 10(c) and (d) (column 3) at $f \sim 3$ Hz (typical time constants of the facility are 1–2 orders lower). This is the result of the existence of slugs. If the amplitude of the volume flow, $A^{f}_{\langle\partial V/\partial t\rangle}(f)$, is observed at high frequencies, there is only a proportional increase, but no change in the functional relationship is obvious. Together with column II it can be supposed that the number of moderate size bubbles ($D_B \sim 5$–10 mm) is increasing, however, their velocity is almost constant. A significant alteration of $A^{f}_{\langle\partial V/\partial t\rangle}$ occurs at low frequencies f: there is the formation of a maximum at $f = 10$–11 Hz which means that most of the gas is transported at this typical frequency. Bubbles that contribute most to the integral void fraction show a maximum in frequency space of the order of 1 Hz, but most of the gas volume is transported at frequencies one-order higher. It must be concluded that a large number of less big bubbles migrate with comparatively high velocities. If this is taken into consideration, the slight slowdown of large slugs, indicated by Figs. 10(c) and (d) (column II), can be explained. However, the explained effect is only latent, it will be the subject of intensive research work in future.

The cited experimental example illustrated the applicability of the wire-mesh tomograph and its useful application for studies on two-phase flow phenomena. However, it has to be taken into consideration that the measuring system is of intrusive nature. The wires act as obstacles and certainly alter the flow. To clarify the quantity of flow modification, studies on a transparent wire-mesh sensor have been performed. This sensor was adapted to geometrical concern from the WMS illustrated in Fig. 2(a) – accordingly, the wire diameter was 0.125 mm and the spatial resolution 2.22×3.03 mm^2. For reasons that were caused by manufacturing demands, the distance between the electrode planes was extended from 1.5 to 2.0 mm. The visual observation has been carried out by use of a high-speed CCD camera, FastCam-Net 500/1000/Max (PHOTRON), equipped with a standard NIKON 100 mm objective. The acrylic channel has been indirectly illuminated with a standard stroboscope and suitably chosen light-diffuser. Sequences have been taken with 1/500 s frame rate, 1/1000 s shutter speed and various apertures.

Three classes of void structures have been investigated: bubbles that have a characteristic size of the order of the WMS mesh size, bubbles that cover significantly more than one mesh size but are still small compared to the hydraulic equivalent diameter of the conduct and finally slugs. Among the phenomenological behaviors of the two groups mentioned first was found as almost identical and is presented in terms of the smallest bubble size in the following. Since the experiments were carried out under atmospheric condition and ambient temperature, specific weighs and surface tension were given values that did not experience any changes. Furthermore, the specific weight of air is only about 1/1000 compared to water, so that changes in the air mass flow will not significantly contribute to the cross-sectional averaged mass flux. The mass flux of the liquid was considered as the most influencing value, due to its direct influence on the equation of momentum conservation.

Observed results are illustrated in Fig. 11 (flow from bottom to top, i.e. upward). The first row shows bubbles and slugs rising in a stagnant liquid, while the second row was experimented at a water mass flux of about 100 kg/m^2 s. In the case of single bubbles, Figs. 11(a) and (d), the influence of adhesive forces is strong in the case of zero-liquid velocity, obvious by the formation of largely elongated wakes after bubble detachment. There is almost no bubble disintegration. In the case of higher liquid velocities the influence of adhesive forces vanishes, but bubbles tend to be disintegrated that can be seen at the smaller bubble sizes downstream the mesh. This cutting of bubbles yields that the measuring volumes are exposed to pure air, Fig. 11(d). Accordingly, the p.d.f. indicating the occurrence frequency of a certain diameter moved towards higher void fraction level

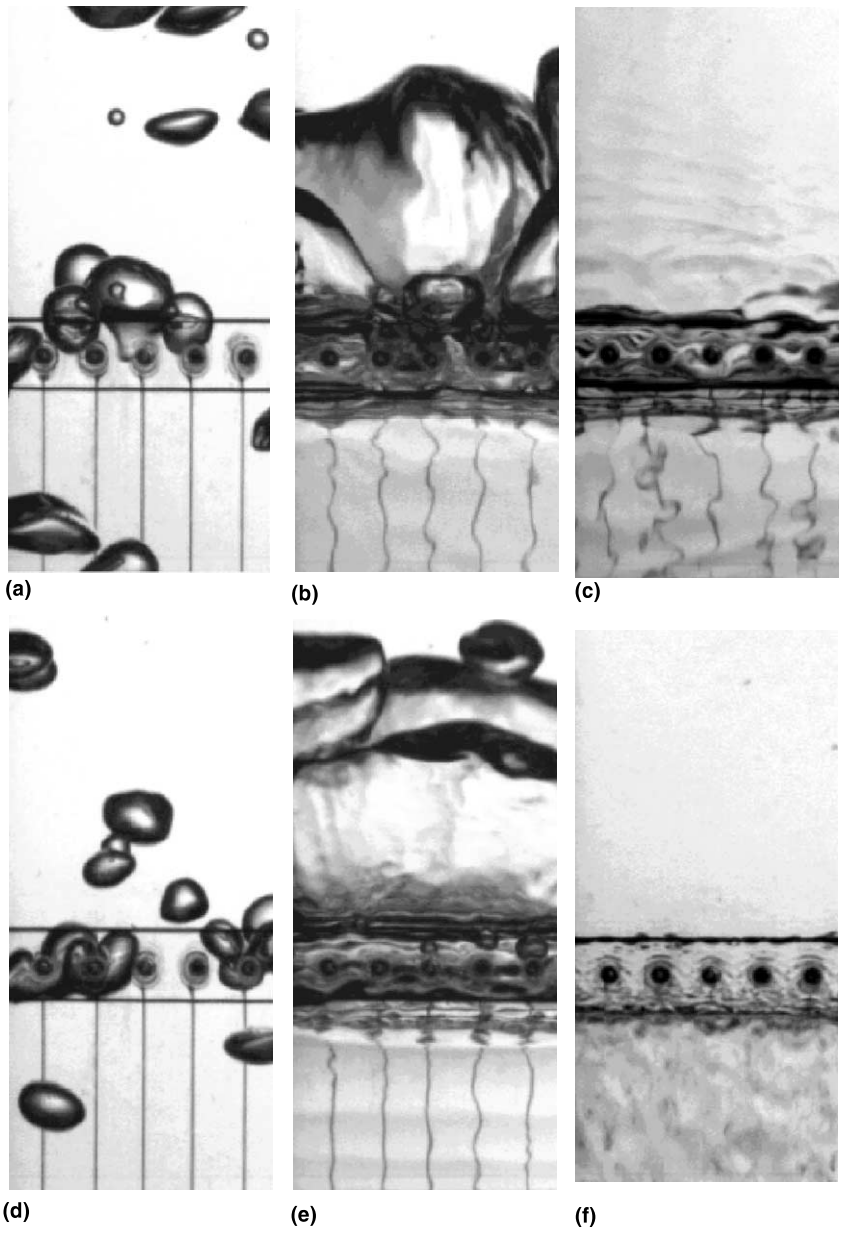

Fig. 11. Bubble–electrode wire interaction: (a)–(c) in stagnant liquid, (d)–(f) liquid mass flux of 100 kg/m^2 s. (a) and (d): single bubbles; (b) and (e) nose of an approaching slug; (c) and (f) film region of a slug.

and becomes sharper, Figs. 4(b) and (d). A deceleration of bubbles could not have been stated, because of almost constant appearance of the normalized void fraction change velocities, Fig. 7(b). While a disintegration of bubbles alters the flow situation only slightly (and as smaller as higher the pressure in the system becomes), a too low water velocity yields a significant lateral bubble movement. Such a movement might yield a kind of blockage and so a dominant modification of a certain flow situation. Since the onset of bubble disintegration was observed at about 100 kg/m^2 s water mass flux, it has been concluded that the sensor cannot be applied to flow situation below this level without significant interaction with the flow field. The measure was found as almost independent of the investigated bubble diameter, i.e. >3 mm. This value has to be understood as sensor-specific and depending on the operation condition.

Similar is the situation for investigated slugs: Figs. 11(b) and (e) show the electrode-mesh interaction with an approaching slug nose (whereby the slug has a mul-

tiple length of the channel width). In all cases a strong interaction can be observed, obvious by a significant deformation of the void structure. However, the expansive movement of the gas in the void structure is strong enough to overcome adhesive forces and maintain a continuously closed bubble. The reconstruction of the original, stable slug form occurs as faster as the slug moves and behaves so proportionally to the liquid speed. The reason therefore is seen in a higher impact of the moved liquid phase around the slug that is much better able to overcome the action of adhesive forces.

In the film region, the WMS also produces little disturbances as illustrated in Figs. 11(c) and (f). Particularly in Fig. 11(f) wave formation forming the amplitude of the wire-diameter can be observed. Most of the waves are directed downstream. Upstream has almost no influence on the obstacle in the case of high flow rates, Fig. 11(f), so that the film remains almost undisturbed. A decrease in the interface velocity, Fig. 11(c), promotes a decrease in the wave number as well as a better propagation of information upstream, obvious by a slight upstream wave formation.

Based on a simultaneous observation of the measured signal by the WMT and the CCD camera taken data, the smallest certainly measurable bubble size was identified as of the electrode plane distance.

In all cases the position of the wires has been found as stable. No mechanical interference could have been stated.

4. Summary

Data processing methods for an electrode-mesh sensor have been proposed. Based on the simultaneous measurement of the local instantaneous void fraction and true gas velocity, a spatial field reconstruction of the gaseous phase has been carried out. This provides information about bubble diameter distribution in its dependency on the true gas velocity, about the distribution of the volume flow over the cross-section as well as about the behavior of cross-sectional averaged void fraction and volume flow in the frequency space.

The flow disturbance by the intrusive device has been clarified and the applicability of the wire-mesh sensor for the applied experimental conditions benchmarked.

The accuracy of the local void fraction measurement was stated as within $\pm 1\%$ in comparison to X-ray data. The true gas velocity and its standard deviation showed up to 5% deviation in comparison to alternatively measured video data for values slower than 500 mm/s. The time averaged gas volume flow through the channel was found within a 10% margin in comparison to data from a laminar flow meter. The true gas velocities did not exceed 500 mm/s for void fractions up to 20%. The qualitative disturbance of the flow by the electrode wires has been discussed.

In general, the applicability of the proposed wire-mesh sensor to spatial field reconstruction has been approved and one interesting example, illustrating the offered possibilities, has been presented. Future work will basically be concentrated on the application of faster sampling hardware components and intensive studies on the characteristics of (transient) bubbly flow under consideration of the developing length.

References

[1] I. Kataoka, A. Serizawa, Statistical behavior of bubbles and its application to the prediction pf phase distribution in bubbly two-phase flow, in: Proceedings of the International Conference on Multiphase Flows'91, vol. 459, Tsukuba, Japan, September 24–27, 1991.

[2] J. Mercier, A. Lyrio, R. Forslund, Three dimensional study of the non rectlinear trajectory of rising air-bubbles in water, Trans. ASME, J. Appl. Mech. 650 (1973).

[3] H.-M. Prasser, A. Böttger, J. Zschau, A new electrode-mesh sensor for gas–liquid flow, Flow Meas. Instr. 9 (1998) 111.

[4] H.-M. Prasser, A. Böttger, J. Zschau, D. Peters, G. Pietzsch, W. Taubert, M. Trepte, Annual Report of Institute of Safety Research, FZR-284, ISSN 1437-322X, 15, 2000.

[5] N. Reinecke, D. Mewes, Recent developments and industrial/research applications of capacitance tomography, Meas. Sci. Technol. 7 (1997) 233.

[6] S. Richter, M. Aritomi, R. Hampel, Methods for studies on bubbly flow using a new wire-mesh tomograph, in: Proceedings of the Second Japanese–European Two-Phase Flow Group Meeting, Tsukuba, Japan, CD-ROM #D-2, September 25–29, 2000.

[7] S. Richter, M. Aritomi, R. Hampel, Algorithm for the application of a new wire-mesh tomograph for advanced studies on bubbly flow characteristics, in: Proceedings of the Fourth Japan–Korea Seminar On Advanced Reactors, vol. 112, Tokyo, Japan, October 19–20, 2000.

[8] M. Sadatomi, Y. Sato, Two-phase flow in vertical noncircular channels, Int. J. Multiphase Flow 8 (1982) 641.

[9] D. Scholz, Forschungszentrum Rossendorf, Wissenschaftlich-Technische Berichte, FZR-300, 56, 2000.